IEEE Access
Multidisciplinary | Rapid Review | Open Access Journal

Received December 11, 2020, accepted December 18, 2020, date of publication December 22, 2020,
date of current version January 5, 2021.

Digital Object Identifier 10.1109/ACCESS.2020.3046500

Estimating the Alumina Concentration During Aluminum Electrolysis by Identifying the Sensitive Frequency Band Using Marginal Kurtosis

ZHAOHUI ZENG[1,2], WEIHUA GUI[1], LIHUI CEN[1], XIAOFANG CHEN[1], AND YONGFANG XIE[1]

[1]School of Automation, Central South University, Changsha 410083, China
[2]Key Laboratory of Intelligent Computing and Information Processing, Ministry of Education, Xiangtan University, Xiangtan 411105, China

Corresponding author: Lihui Cen (lhcen@csu.edu.cn)

This work was supported in part by the National Natural Science Foundation of China under Grant 61773405, Grant 61751312, and Grant 61533020; and in part by the Major Scientific and Technological Innovation Projects of Shandong Province under Grant 2019JZZY020123.

ABSTRACT The accurate and timely online estimation of the alumina concentration in an industrial aluminum electrolysis cell can improve its feed control performance. By using the proposed marginal kurtosis (MK), marginal kurtosis dominant frequency (MK-DF), integral feed frequency and sensitive frequency band (SFB), this study reveals that a normalized cell voltage with different current intensities and feed schemes has different alumina concentration SFBs and determines the general formula for calculating the SFB. On this basis, a general algorithm for acquiring the pseudo alumina concentration (PAC) using translation-invariant filtering is proposed in which the upper limit of the SFB provides the cutoff frequency of the low-pass filter. The PAC was used to estimate the absolute and relative concentrations of alumina. The absolute concentrations are validated using measured concentrations. Additionally, improved feed control performance of the industrial cells is presented using the relative concentration PAC-slope.

INDEX TERMS Aluminum electrolysis, integrated feed frequency, marginal kurtosis, marginal kurtosis dominant frequency, pseudo alumina concentration, sensitive frequency band.

NOTATIONS

$[0, f_{sens}]$	Alumina concentration sensitive frequency band, SFB.
$[g\ h]$	Wavelet and scaling filter coefficients of db2.
$[C_{\mathrm{AE}},\ C_{\mathrm{ThLow}}]$	Controllable zone of the alumina concentration.
$[g_{J_0}\ h_{J_0}]$	J_0th level TIDWT wavelet and scaling filters of db2.
α	The loss rate of alumina during feeding.
η	Current efficiency.
C	Alumina concentration.
$g(\cdot)$	Nonstationary signal.
I	Sample cell current.
J, J_0	Transform level of the partial TIDWT.
L	Support length of an orthonormal wavelet.
$M_K^{(1)}$	The first derivative of $M_K(f)$.
$M_K^{(2)}$	The second derivative of $M_K(f)$.
N	Length of the original signal.
r	Vanishing moments of an orthonormal wavelet.
s	Feed factor.
β_o	Overfeed percentage.
β_u	Underfeed percentage.
$\mathrm{G}^{(1)}$	The first derivative of G.
$\mathrm{G}^{(2)}$	The second derivative of G.
$\mathrm{G}_{\mathrm{K0009}}$	The slope obtained by using the multiple filters method.
$\mathrm{G}'_{\mathrm{K0009}}$	The forward shifting of $\mathrm{G}_{\mathrm{K0009}}$.
$\mathrm{G}_{\mathrm{T}f_{filter}}$	The change rate of resulting components filtered by using the db2 partial TIDWT for the frequency band $[0, f_{filter}]$ Hz.

The associate editor coordinating the review of this manuscript and approving it for publication was Shafiqul Islam.

P_{uo}	Slope threshold for transition of underfeed to overfeed.
$\tilde{s}_{feed}$	Default single feed amount.
C_{AE}	Critical alumina concentration.
C_{PAC}	Pseudo alumina concentration, PAC.
C_{ThLow}	Alumina concentration corresponding to U_{ThLow}.
D_{feed,F_N}	Duration time vector F_N.
$D_{ifp,F_N}(i)$	Duration of the ith practical-IFP of F_N.
D_{ofdMax}	Maximum overfeed duration.
D_{ofd}	Overfeed duration.
D_{Thfeed}	Theoretical integrated feed period duration, Theoretical-IFP duration.
D_{ufdMax}	Maximum underfeed duration.
D_{ufd}	Underfeed duration.
E_c	Pseudo counter electromotive force.
F_c	The rate of alumina consumption per second.
f_d	Dominant frequency based on the Marginal kurtosis of $g(\cdot)$, MK-DF.
f_{feed,F_N}	Practical-IFF vector of F_N.
f_{filter}	Frequency upper limit of the pass-band of the scaling filter.
$f_{ifp,F_N}(i)$	The ith practical integrated feed frequency of F_N, ith practical-IFF.
f_s	Sampling frequency.
f_{Thfeed}	Theoretical integrated feed frequency, Theoretical-IFF.
F_{Uj}, F_N	Feed state corresponding to Uj and U_N, respectively, FDS.
G_{PAC}	The change rate of PAC, PAC-slope.
g_{feed}	Capacity of the feeder.
$h_g(x)$	Hilbert transform of the nonstationary signal Hilbert transform of the nonstationary signal.
I_b	Basic line current.
k_1	Transition factor 1.
k_2	Transition factor 2.
L_j	Length of the jth level TIDWT wavelet and scaling filters.
M_{feed,F_N}	Practical integrated feed matrix of F_N, practical-IFM.
$M_K(f)$	Marginal kurtosis of $g(\cdot)$, MK.
n_{feed}	Number of feeders.
n_{ifp}, n_{ifp,F_N}	The number of practical-IFPs in F_N.
$N_{oThfeed}$	Theoretical overfeed interval.
N_{Thbase}	Theoretical basic feed interval, theoretical-BFI.
$N_{uThfeed}$	Theoretical underfeed interval.
R_0	Pseudo cell resistance.
s_{feed}	Amount of single feed.
S_{F_N}	Feed state set.
$T_{ifp,F_N}(i)$	The ith practical integrated feed period of F_N, ith practical-IFP.
$t_{oe}(i)$	End position of the ith overfeed period.
$t_{os}(i)$	Start position of the ith overfeed period.
$t_{ue}(i)$	End position of the ith underfeed period.
$t_{us}(i)$	Start position of the ith underfeed period.
U_N, Uj	Normalized cell voltage, NCV.
U_S	Sample cell voltage.
U_{ThLow}	Minimum value of the theoretical cell voltage.
U_{Th}	Theoretical cell voltage.
V_{J_0}	Scale coefficients of the level J_0 db2 TIDWT-based.
$W_g(t,f)$	Integral wavelet transform of $h_g(x)$.
ACD	Anode cathode distance.
ARE	Average relative error.
BFI	Basic feed interval.
DWT	Discrete wavelet transform.
IWT	Integral wavelet transform.
MRA	Multi-resolution analysis.
PSD	Power spectral density.
RMSE	Root mean square error.
TI	Translation invariant.
WPT	Wavelet-packet transform.

I. INTRODUCTION

The alumina concentration is a crucial parameter to ensure efficient and green production during the aluminum electrolysis process [1], [2]. The refined feed control of the alumina concentration depends on the accuracy and timeliness of the online estimation of this concentration, which is of great significance for improving product quality and reducing energy consumption and greenhouse gas emissions. Due to the lack of sensors that can meet the requirements of industrial control for online measurement of the alumina concentration, fast online measurement of this concentration is currently not available.

The cell voltage changes with the alumina concentration. The slope, which is calculated from the component related to the alumina concentration extracted from the cell voltage measured online, is the main basis for alumina feed control [3]–[5] in an industrial cell. Therefore, whether the extracted component represents the alumina concentration change in an accurate and timely manner directly affects the performance of control system. In past decades, multiple Kalman filters [3], [6], [8] and other multiple filters were commonly used to analyze the cell voltage (or cell resistance). For example, reference [8] used recursive low-pass digital filters and multiple Kalman filters to obtain the change rate of the filtered cell resistance for alumina feed control, in which the filter coefficients and the number of cascaded filters were determined by experience or on-site experiments. In [7], the power spectrum and amplitude spectrum of the normalized cell voltage (NCV) of a 160-kA prebaked anode cell with point feeders were studied using the fast Fourier transform, in which the filter pass-band for alumina concentration online control is $\left[0,\ 2\times10^{-3}\right]$ Hz. With increasing electrolysis intensity, it has appeared diverse sizes (with different current intensities) of industrial cells have appeared, such as 200-kA, 400-kA, 500-kA and 600-kA cells. Moreover, two cells with the same cell size may have different feeding schemes. There is a certain lag in the filtered voltage obtained by the cascade

of the multiple filter method. Additionally, the filtered voltage, which is obtained by using the filter pass-band and filter coefficients determined by experiment or experience, still contains much noise. Thus, using the relative alumina concentration (called the slope) calculated from the filtered voltage as the primary basis will cause the feed control decision to lag behind the alumina concentration change, or even result in incorrect control decisions.

To estimate the online alumina concentration in an accurate and timely manner and improve the performance of the feed control system of industrial cells, this paper combines process mechanism analysis, signal analysis and material balance theory and proposes concepts such as the MK, MK-DF, integrated feed frequency (IFF), alumina concentration sensitive frequency band (SFB) and pseudo alumina concentration (PAC). Most of these parameters are derived from the cell voltage. The identification of the SFB using MK provides the narrower pass-band for filter design and contributes to reducing the control system complexity and the occurrence of incorrect control decisions, both of which are caused by using an experience-based pass-band. The introduction of translation-invariant filtering can overcome the drawbacks of frequency aliasing and delay caused by the cascade of multiple filters. Both the SFB and translation-invariant filtering can improve the accuracy and timeliness of alumina concentration estimation and feed control performance.

The rest of this study is organized as follows. In section II, the feature of NCV is analyzed by using MK and MK-DF. In section III, the SFB is identified by MK-DF and IFF. In section IV, the general calculation algorithm for the PAC is proposed, and measured concentrations are used to validate those estimated by the PAC. In section V, the improvement of the feed control performance is presented. Finally, section VI presents the conclusions.

II. ANALYSIS OF NCV

The normalized cell voltage is the practical control signal in industrial aluminum electrolysis. In this section, by using the process mechanism knowledge, the ''under-rise and over-fall'' relationship between the NCV and the feed state for the normal alumina concentration condition is verified [3]. After defining the MK and MK-DF, the frequency corresponding to the NCV energy peak is obtained. Then, the MK and MK-DF method are compared with common frequency identification approaches, such as spectral analysis and spectral kurtosis [9]–[11].

A. PROCESS MECHANISM ANALYSIS

Reference [12] proposed the relationship between the theoretical cell voltage U_{Th} and the alumina concentration C, which was described as the U-curve, shown in Fig. 1. On the U-curve, the theoretical cell voltage has a minimum value U_{ThLow} corresponding to the concentration C_{ThLow}. When the alumina concentration is above or below C_{ThLow}, the cell voltage increases. On the left side of C_{ThLow}, the cell voltage increases significantly as the concentration decreases. When

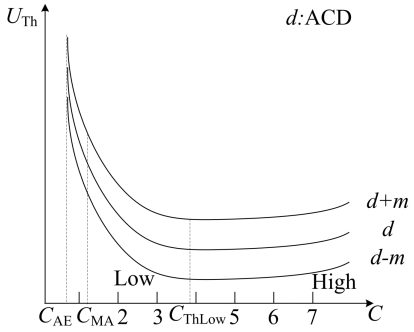

FIGURE 1. Qualitative relationship among the theoretical cell voltage, alumina concentration and ACD.

the concentration is lowered to the critical concentration C_{AE}, the cell voltage rises sharply, and the anode effect will occur. The interval (C_{AE}, C_{ME}) of the alumina concentration is called the multi-effect zone, which indicates a very low alumina concentration where anode effects frequently occur; The interval (C_{ME}, C_{ThLow}) is called the controllable zone, which indicates a normal alumina concentration. The U-curve shows that the theoretical cell voltage is sensitive to concentration changes when the alumina concentration is in the normal range.

In Fig. 1, an adjustment of the anode-cathode distance (ACD) may cause the U-curve to drift up and down, and a temperature change may cause it to shift left and right. In industrial cells, the ACD, bath temperature and components change in real time and are thus unavailable for online measurement and quantitative calculations, resulting in the difficulty of establishing accurate mathematical models suitable for online control of the cell voltage and alumina concentration. Fortunately, the shape of the U-curve is basically stable, although its position is variable and cannot be quantitatively calculated. Therefore, the slope calculated from the cell voltage (or the cell resistance) is regarded as the relative alumina concentration, both in academia and industry, which is further used in alumina feed control [4], [13], bath temperature control [14], anode effect forecasting [3], [15] and so on. Thus, the performance of the control system is directly determined by whether the slope accurately represents the concentration change.

To eliminate the interference caused by line current changes, the normalized cell voltage $U_{\mathrm{N}}(k)$ is used as the critical signal in the cell control system, i.e.

$$U_{\mathrm{N}}(k) = R_0(k)I_b + E_c = \frac{U_{\mathrm{S}}(k) - E_c}{I_{\mathrm{S}}(k)} I_b + E_c \qquad (1)$$

In (1), $R_0(k) = \frac{U(k)-E_c}{I(k)}$ is the pseudo cell resistance at time t_k, $U_{\mathrm{S}}(k)$ is the sample cell voltage, $I(k)$ is the sample cell current, I_b is the basic line current, and E_c is the pseudo counter electromotive force.

Fig. 2(a) shows the NCV $U1$ (NCV, magenta) and the feed state F_{U1} (FDS, red) of a 400-kA cell with the left side of the U-curve as the target control zone. $U1$ and F_{U1}

have a sampling frequency of $f_s = \frac{1}{\Delta t} = 0.1$ Hz (an effective frequency band of [0, 0.05] Hz) and a length of $N = 1440$. When collecting the data, the cell condition is normal (referred to as the normal cell condition): there is no routine operation of metal tapping, anode change or beam raising, no special operations such as edge processing, no anode movement, and no anode effect or any other special cell conditions. A high position of F_{U1} indicates an underfeed period, and a low level indicates an overfeed period; the labels on F_{U1} indicate the sequence positions of the underfeed/overfeed switch. As shown in Fig. 2(a),

1) In the underfeed period, the practical feed amount of alumina is lower than the theoretical consumption, causing the concentration to gradually decrease. Then, $U1$ gradually rises, which illustrates the definition of the "under-rise".
2) In the overfeed period, the practical feed amount of alumina is higher than the theoretical consumption, causing the concentration to gradually increase. Then, $U1$ falls, which illustrates the definition of the "over-fall".

It can be concluded that if the concentration is within the normal range, the NCV and the feed state have a relationship of "under-rise and over-fall" [3], which is consistent with the mechanism analysis in [12], [16], [17]. This study will use "under-rise and over-fall" as the basis for judging the normality of the alumina concentration.

Therefore, the NCV contains alumina concentration information and can track the concentration change. Unlike the theoretical cell voltage, the NCV collected from industrial cells is a complex, nonstationary signal containing multiple frequency components [7], [18]–[20], which cannot be directly used for alumina concentration estimation.

B. ANALYSIS OF NCV USING MK AND MK-DF

To find the frequency bands related to the alumina concentration information in the NCV, this subsection takes $U1$ as an example to study the frequency characteristics of the NCV and prepare for the identification of the alumina concentration SFB. Different from the previous approach [7], this subsection first analyzes the time-frequency characteristics of the NCV by using the integral wavelet transform (IWT) and then captures the frequency of the NCV energy accumulation by defining the MK and MK-DF. Finally, this frequency identification method is compared with other commonly used methods of finding the interested frequency, such as power spectrum density (PSD) and spectral kurtosis (SK).

1) DEFINITION OF MK

The amplitude analysis of the integral wavelet transform (IWT) of $U1$ in the range of [0, 0.05] Hz shows that the energy has distinct distributions in the high-frequency and low-frequency region, and concentrates mainly in the low-frequency region. Fig. 2(b) presents a zoom-in view of [0, 0.01] Hz, which shows that there are no obvious singular values in the low-frequency region.

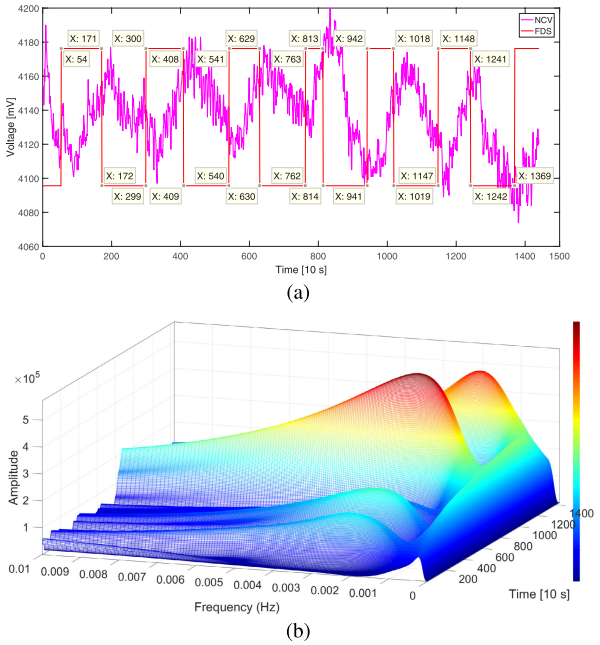

FIGURE 2. (a) $U1$ and F_{U1}; (b) Energy distribution of $U1$ in [0, 0.01] Hz.

To further analyze the NCV and find the determined frequency corresponding to the energy peak of NCV, this study proposes the MK and MK-DF.

Let $h(x)$ be the Hilbert transform of the nonstationary signal $g(\cdot) \in \mathrm{L}^2(\mathrm{IR})$; then, the integral wavelet transform of $h(x)$ is

$$W_g(b,a) = |a|^{-\frac{1}{2}} \int h(x) \cdot \overline{\psi(\frac{x-b}{a})} \cdot dx \tag{2}$$

Define $g(\cdot)$'s marginal kurtosis as

$$M_K(f) \equiv \frac{\int_{-\infty}^{+\infty} \left|W_g(t,f)\right|^2 \cdot dt}{\int_{-\infty}^{+\infty} \int_{-\infty}^{+\infty} \left|W_g(t,f)\right|^2 \cdot dt \cdot df} \tag{3}$$

Let $M_K(f)$ be the marginal kurtosis of $g(\cdot) \in \mathrm{L}^2(\mathrm{IR})$; if $M_K^{(1)}(f_d) = 0$ and $M_K^{(2)}(f_d) < 0$, then f_d is the dominant frequency based on marginal kurtosis of $g(\cdot)$.

Equations (2) and (3) show that marginal kurtosis is the normalized frequency marginal distribution of the integral wavelet transform energy of $h(x)$, and the MK-DF is the frequency corresponding to the local maximum of the MK.

2) ESTIMATION OF MK-DF

Fig. 3(c) shows the MK of $U1$. In Fig. 3(c), (1) the energy of $U1$ is mainly concentrated in the low-frequency region of the effective frequency band and gradually decays to the high-frequency region; (2) in the range of [0, 0.01] Hz, $U1$ has a local maximum, which is recorded as the MK-DF1, $f_{d1} = 0.0003$ Hz; and (3) above 0.001 Hz, there is also a local maximum, which is recorded as MK-DF2, $f_{d2} = 0.0002$ Hz. These two MK-DFs correspond to the energy accumulation frequencies below and above 0.001 Hz in Fig. 2(b), respectively.

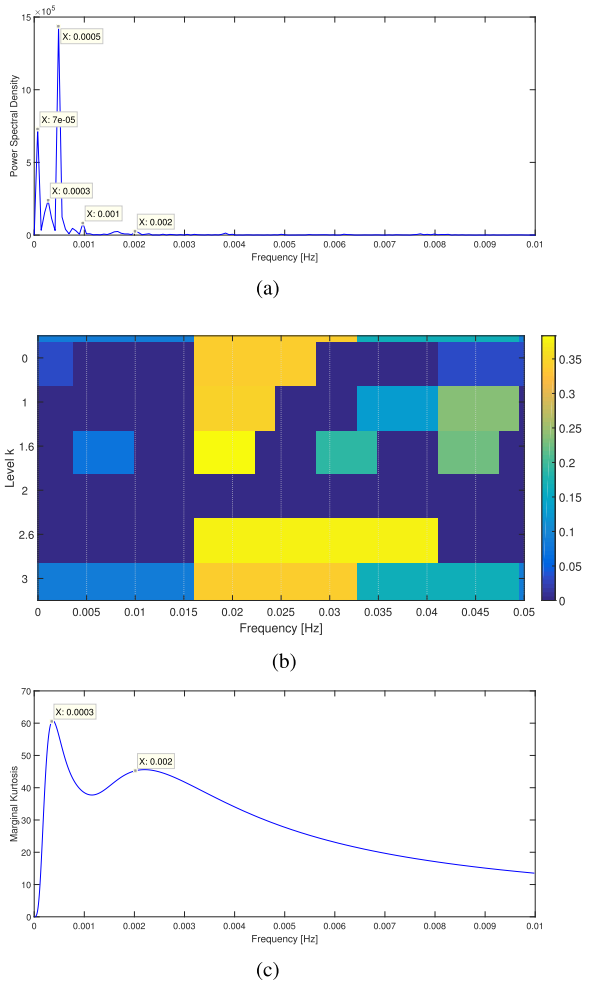

FIGURE 3. Analysis of $U1$ (a) PSD; (b) Spectral kurtosis; (c) Marginal kurtosis.

Fig. 3(a) shows the PSD of $U1$ in the range [0, 0.01] Hz. Fig. 3(b) shows the spectral kurtosis of $U1$, based on spectral kurtosis algorithms. As shown in Fig. 3(a), the PSD has several peaks below 0.001 Hz, but only one peak is the same as the MK-DF f_{d1}; there are no apparent spectral peaks above 0.001 Hz. Fig. 3(b) shows that the SK is insensitive to the time-frequency characteristics of $U1$ and has a large value (shown in yellow) throughout the low-frequency region.

Since the PSD lacks the statistical properties of the signal and is prone to generate a pseudo spectral peak, and the SK is insensitive to the energy aggregation of nonsingular signals, they are not as suitable for signal analysis as the NCV. The proposed MK based on the integral wavelet transform can find the energy aggregation frequencies of the NCV. Therefore, the MK is more suitable for analyzing complex signals, which have energy concentrated in nonsingular frequency components, representing a useful supplement to PSD and SK analysis.

3) MK-DF OF THE NCV WITH VARIOUS CELL CONDITIONS

This subsection also uses MK and MK-DF to perform systematic analysis on the NCV under various cells conditions

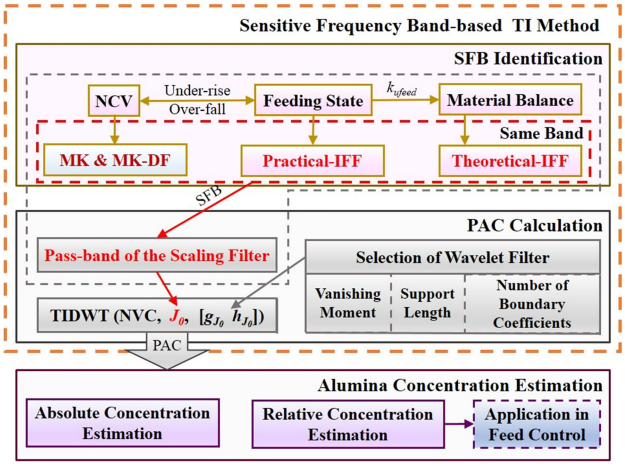

FIGURE 4. Framework for alumina concentration estimation based on SFB identification.

and obtains the general frequency characteristics of the NCVs that basically satisfy the "under-rise and over-fall" relationship. For example, $U2$ prior to the anode effect and $U3$ after the metal tapping are analyzed (see Appendix Fig. 16 and Fig. 17). The MK-DFs of many NCVs that basically conform to the "under-rise and over-fall" relationship with the previous three cell conditions are calculated. Then the sets $\{f_{d1}\}$ and $\{f_{d2}\}$ are obtained. (see Appendix Table 4, Table 5, and Table 6.)

The result shows that the vast majority of the NCVs have MK-DF f_{d1} below 0.001 Hz and that some NCVs also have MK-DF f_{d2} above 0.001 Hz. The MK accurately captures the frequency characteristics of the NCV, which lays a good foundation for subsequent SFB identification. In section III, it is further determined that one of the MK-DFs is related to changes in the alumina concentration.

C. FRAMEWORK FOR ALUMINA CONCENTRATION ESTIMATION BASED ON IDENTIFICATION OF THE SFB

Fig. 4 presents the overall framework of this article, which is divided into three parts: in the first part, MK and MK-DF are used to identify the SFB of alumina concentration in NCV; in the second part, the translation-invariant (TI) method is used to acquire PAC from NCV, which can accurately represent the alumina concentration; and in the third part, the absolute concentration and the relative concentration PAC-slope are estimated based on the PAC, where the relative concentration PAC-slope is the primary basis for feed control in an industrial cell. The first part and the second part (in the yellow dotted box) constitute a sensitive frequency band-based TI method for acquiring the PAC.

In the SFB identification part, the alumina concentration change period is analyzed from three different perspectives, namely, NCV, feed state, and material balance, to determine the SFB $[0, f_{sens}]$ Hz that is sensitive to the change in alumina concentration in the NCV. The results of these three analysis perspectives are as follows:

(1) From the NCV perspective, the first two sections of this chapter use the proposed MK and MK-DF to analyze the

frequency characteristics of a large number of NCVs when the alumina concentration is basically normal under various operating conditions.

(2) The first section of Chapter 3 defines the formal expression of the practical integrated feed frequency (practical-IFF) from the perspective of the feed state controlling the change in the alumina concentration, and the calculation formula of the practical-IFF is given.

(3) The second section of Chapter 3 defines the theoretical integrated feed frequency (theoretical-IFF) from the perspective of material balance and gives its calculation formula.

According to the subsequent analysis, those of the MK-DF set, the practical-IFF set and the theoretical-IFF are basically in the same frequency band (shown in the red dotted box in Fig. 4). Therefore, instead of by experience or the on-site experimental method, a formula for calculating the SFB $[0, f_{sens}]$ is given on the basis of the theoretical-IFF.

In the PAC calculation part, (1) f_{sens} is used as the cutoff frequency of the low-pass filter that acquires the alumina concentration information from the NCV (shown by the gray dashed box in Fig. 4). (2) Based on the properties of the vanishing moment, compact support, and boundary coefficients, the optimal wavelet filter is selected. (3) To reduce the delay of multiple filter cascade filtering, this study uses translation-invariant filtering in calculating the PAC.

In the alumina concentration estimation part, the estimations of absolute and relative concentration are made. Then, the relative concentration the PAC-slope obtained in this study and the slope used in the industrial field are used to compare the performance of feed control.

III. IDENTIFICATION OF SFB BASED ON MK AND IFF

In this section, the practical integrated feed frequency (practical-IFF) and the practical integrated feed period (practical-IFP) of the feed state are proposed, and their formal representations are given; the theoretical integrated feed frequency (theoretical-IFF) and the theoretical integrated feed period (theoretical-IFP) calculation formulas are then derived according to the material balance principle. Then, one of the MK-DFs is proven to be related to the alumina concentration from the aspects of NCV, feed state, and material balance theory. Finally, the general formula for calculating the alumina concentration SFB is given.

A. PRACTICAL-IFF FORMAL REPRESENTATION OF THE FEED STATE

The alumina feed directly affects the alumina concentration in industrial cells. To obtain more online alumina concentration information, this subsection defines the practical-IFF and the practical-IFP of the feed state.

Normally, the time of the end of underfeed and the beginning of overfeed is the period of the lowest alumina concentration, when the NCV is highly susceptible to a change in the alumina concentration. To make this susceptive period the focus of the analysis, the practical integrated feed period (practical-IFP) is defined as follows. Let F_N be the feed state series with the sample interval of Δt corresponding to U_N. Define the ith underfeed period of F_N and the next overfeed period as the ith practical integrated feed period (practical-IFP) of F_N, denoted by the quaternion

$$T_{ifp,F_N}(i) \equiv \begin{pmatrix} t_{us}(i) & t_{ue}(i) & t_{os}(i) & t_{oe}(i) \end{pmatrix} \tag{4}$$

In (4), $t_{us}(i), t_{ue}(i), t_{os}(i), t_{oe}(i) \in \mathrm{N}^+$, $t_{us}(i)$ is the start position of the ith underfeed period, $t_{ue}(i)$ is the end of the ith underfeed period, $t_{os}(i)$ is the start of the ith overfeed period, and $t_{oe}(i)$ is the end position of the ith overfeed period. $t_{os}(i) = t_{ue}(i) + k_1$ and $t_{us}(i+1) = t_{oe}(i) + k_2$, $k_1, k_2 \in \mathrm{N}^+$. k_1 is transition factor 1, indicating the number of sampling points used in the underfeed $t_{us}(i)$ to transition to the overfeed $t_{os}(i)$ in the ith practical-IFP; k_2 is transition factor 2, indicating the number of sampling points during the period from the end of overfeed $t_{oe}(i)$ in the ith practical-IFP to the start of underfeed $t_{ue}(i+1)$ in the $(i+1)$th practical-IFP, where $t_{us}(i) < t_{ue}(i) < t_{os}(i) < t_{oe}(i)$. Thus, the alumina concentration is lowest near the switch point in each practical-IFP when underfeed switches to overfeed.

Define the length of the ith practical-IFP to be the difference between the end position of the overfeed and the start position of the underfeed: $\left|T_{ifp,F_N}(i)\right| \equiv t_{oe}(i) - t_{us}(i) + 1$, $\left|T_{ifp,F_N}(i)\right| \in \mathrm{N}^+$, then $D_{ifp,F_N}(i) \equiv \left|T_{ifp,F_N}(i)\right| \cdot \Delta t$, $D_{ifp,F_N}(i) \in \mathrm{R}^+$, is the duration of the ith practical-IFP, and the ith practical-IFF is $f_{ifp,F_N}(i) \equiv \frac{1}{D_{ifp,F_N}(i)} = \frac{1}{\left|T_{ifp,F_N}(i)\right| \cdot \Delta t}$, $f_{ifp,F_N}(i) \in \mathrm{R}^+$. If there are n_{ifp} practical-IFPs in F_N, define the practical integrated feed matrix (practical-IFM) of F_N as

$$M_{feed,F_N} \equiv \begin{bmatrix} T_{ifp,F_N}(1) & T_{ifp,F_N}(2) & \cdots & T_{ifp,F_N}(n_{ifp}) \end{bmatrix}^{\mathrm{T}} \tag{5}$$

In (5), M_{feed,F_N} is an $n_{ifp} \times 4$ matrix, $n_{ifp} \in \mathrm{N}^+$.

Define the duration time vector D_{feed,F_N} and the practical-IFF vector f_{feed,F_N} of the feed state F_N as

$$\begin{aligned} D_{feed,F_N} &\equiv \begin{bmatrix} D_{ifp,F_N}(1) & D_{ifp,F_N}(2) & \cdots & D_{ifp,F_N}(n_{ifp}) \end{bmatrix}^{\mathrm{T}} \\ &= \Delta t \times \left(M_{feed,F_N} \times \begin{bmatrix} -1 & 0 & 0 & 1 \end{bmatrix}^{\mathrm{T}} + 1_{n_{ifp} \times 1}\right) \end{aligned} \tag{6}$$

$$\begin{aligned} f_{feed,F_N} &\equiv \begin{bmatrix} f_{ifp,F_N}(1) & f_{ifp,F_N}(2) & \cdots & f_{ifp,F_N}(n_{ifp}) \end{bmatrix}^{\mathrm{T}} \\ &= \begin{bmatrix} \frac{1}{D_{ifp,F_N}(1)} & \frac{1}{D_{ifp,F_N}(2)} & \cdots & \frac{1}{D_{ifp,F_N}(n_{ifp})} \end{bmatrix}^{\mathrm{T}} \end{aligned} \tag{7}$$

A large number of feed states, corresponding to those NCVs with an "under-rise and over-fall" relationship in section II, are selected to constitute a feed state set S_{F_N}. By using (6) and (7), the practical-IFMs set $\{M(S_{F_N})\}$ and the practical-IFFs set $\{f_{ifp}(S_{F_N})\}$ are obtained.

B. THEORETICAL-IFF CALCULATION BASED ON MATERIAL BALANCE THEORY

This subsection analyzes the influencing factors of the alumina concentration from the perspective of material balance and derives the formula for calculating the theoretical-IFF under ideal conditions to prepare for the identification of the SFB.

Let the current intensity be I, the current efficiency be η, and the loss rate of alumina during feeding be α. Based on the electrochemical equivalent and theoretical aluminum production, the rate of alumina consumption per second is

$$F_c = 1.7617 \times I \times \eta \times (1+\alpha) \times 10^{-4} \tag{8}$$

where $\eta, \alpha \in (0, 1]$, η and α are preset values, e.g. $\eta = 0.93$, $\alpha = 0.02$.

Let the capacity of the feeder be $g_{feed} \in \mathrm{R}^+$ and the number of feeders be $n_{feed} \in \mathrm{N}^+$ and define the amount of single feed as $s_{feed} \in \mathrm{R}^+$,

$$s_{feed} \equiv \frac{g_{feed} \cdot n_{feed} \cdot s}{\eta \cdot (1+\alpha)} \tag{9}$$

In (9), $s \in (0, 1]$ is the feed factor. For single-point feed, $s = \frac{1}{n_{feed}}$; for an alternate feed, $s = \frac{1}{2}$; and for simultaneous feed, $s = 1$. The single-feed amount for each feed is determined by adjusting s according to the operation condition. The default single-feed amount $\tilde{s}_{feed} \in (0, 1]$, related to the default feed factor $\tilde{s}$ is called the feed scheme. Then, the theoretical basic feed interval (theoretical-BFI) N_{Thbase} is defined as

$$\begin{aligned} N_{Thbase} &\equiv \frac{g_{feed} \cdot n_{feed} \cdot \tilde{s}}{F_c} \\ &= \frac{g_{feed} \cdot n_{feed} \cdot \tilde{s} \cdot 10^4}{1.7617 \times I \times \eta \times (1+\alpha)} = \frac{\tilde{s}_{feed} \cdot 10^4}{1.7617 \times I} \end{aligned} \tag{10}$$

Let the underfeed percentage be β_u, $\beta_u \in [0, 1)$ and the overfeed percentage be β_o, $\beta_o \in [0, 1]$; then, the theoretical underfeed interval $N_{uThfeed}$ and the theoretical overfeed interval $N_{oThfeed}$ are

$$N_{uThfeed} = \frac{N_{Thbase}}{(1-\beta_u)}, N_{oThfeed} = \frac{N_{Thbase}}{(1+\beta_o)} \tag{11}$$

where $N_{uThfeed}, N_{oThfeed} \in \mathrm{R}^+$.

In this way, the underfeed duration D_{ufd} and the overfeed duration D_{ofd} can be defined as

$$D_{ufd} \equiv N_{uThfeed} \cdot k_{ufeed} = \frac{N_{Thbase} \cdot k_{ufeed}}{1-\beta_u} \tag{12}$$

$$D_{ofd} \equiv N_{oThfeed} \cdot k_{ofeed} = \frac{N_{Thbase} \cdot k_{ofeed}}{1+\beta_o} \tag{13}$$

where k_{ufeed}, $k_{ofeed} \in \mathrm{N}^+$ are the underfeed coefficient and the overfeed coefficient; $D_{ufd} \le D_{ufdMax}$, D_{ufdMax} is the maximum underfeed duration; and $D_{ofd} \le D_{ofdMax}$, D_{ofdMax} is the maximum overfeed duration. Define the theoretical-IFP duration D_{Thfeed} as the sum of the underfeed duration and the next overfeed duration based on the theoretical basic feed interval, i.e.,

$$D_{Thfeed} \equiv D_{ufd} + D_{ofd} \tag{14}$$

Then, the theoretical-IFF f_{Thfeed} is

$$f_{Thfeed} \equiv \frac{1}{D_{Thfeed}} \tag{15}$$

where $D_{Thfeed}, f_{Thfeed} \in \mathrm{R}^+$.

Ideally, the theoretical consumption of alumina in the theoretical-IFP is equal to the cumulative addition, i.e., $F_c \cdot D_{Thfeed} = (k_{ufeed} + k_{ofeed}) \cdot g_{feed} \cdot n_{feed}$, and then,

$$k_{ofeed} = \left\lceil k_{ufeed} \cdot \frac{1+\beta_o}{1-\beta_u} \right\rceil \tag{16}$$

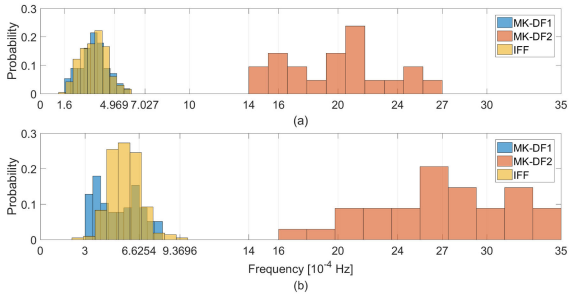

FIGURE 5. Histograms for two sizes of cells (a) 400-kA; (b) 200-kA.

Substituting (8), (10), (11), (12), (13), (14), and (16), into (15), then $D_{Thfeed} = 2 \cdot N_{Thbase} \cdot \frac{k_{ufeed}}{1-\beta_u}$, i.e.,

$$f_{Thfeed} = \frac{1.7617 \times I \times (1-\beta_u) \times 10^{-4}}{2 \cdot \tilde{s}_{feed} \cdot k_{ufeed}} \tag{17}$$

where $f_{Thfeed} \in \mathrm{R}^+$, β_u is constant, and k_{ufeed} is the number of feed times in the minimum underfeed period in the feed state set S_{F_N}.

Equation (17) indicates that the theoretical-IFF in the ideal state is directly proportional to the current intensity I and inversely proportional to the feed scheme $\tilde{s}_{feed}$.

C. IDENTIFICATION OF THE ALUMINA CONCENTRATION SFB

This subsection will analyze the NCVs of 400-kA and 200-kA cells, and obtain $\{f_{d1}\}$, $\{f_{d2}\}$, $\{f_{ifp}(S_{F_N})\}$ and f_{Thfeed} for these two types of cells, respectively. Finally, it is determined that the SFB covers the sets $\{f_{d1}\}$ and $\{f_{ifp}(S_{F_N})\}$ and varies with the current intensity I and the feed scheme $\tilde{s}_{feed}$.

Fig. 5(a) depicts a histogram of the sets $\{f_{d1}\}$, $\{f_{d2}\}$ and $\{f_{ifp}(S_{F_N})\}$ in a 400-kA cell, where $\{f_{d1}\}$ is shown by the blue histogram, $\{f_{d2}\}$ by the red histogram, and $\{f_{ifp}(S_{F_N})\}$ by the yellow histogram. The abscissa $f_{Thfeed} = 4.9690 \times 10^{-4}$ Hz is the theoretical-IFF under ideal conditions determined by (17). Fig. 5(b) shows the histogram of the sets of the 200-kA cell obtained by the same method, and the theoretical-IFF $f_{Thfeed} = 6.6254 \times 10^{-4}$ Hz under ideal conditions.

Fig. 5 shows the following,

(1) For both the 400-kA cell and the 200-kA cell, the set $\{f_{d1}\}$ (MK-DF1, shown in blue) is in almost the same range as the set $\{f_{ifp}(S_{F_N})\}$ (IFF, shown in yellow), and both are distributed around the frequency $f_{Thfeed} = 4.969 \times 10^{-4}$ Hz or $f_{Thfeed} = 6.6254 \times 10^{-4}$ Hz.

When the cell condition is normal, the feed state determines the alumina concentration. Because the range of the set $\{f_{ifp}(S_{F_N})\}$ is substantially the same as the set $\{f_{d1}\}$, it is the MK-DF1 that relates to the frequency band, which is associated with the alumina concentration component in the NCV.

In Fig. 5, the sets $\{f_{d1}\}$ and $\{f_{ifp}(S_{F_N})\}$ are distributed around the frequency f_{Thfeed}. In fact, the practical basic feed interval (practical-BFI) N_{base} is adjusted around the theoretical-BFI N_{Thbase} according to certain cell conditions, and the change in k_{ufeed} depends on the relative concentration, namely, the slope, which varies with the cell condition.

Additionally, the cell condition, including the retention of alumina on the shell surface or the collapse of the shell, the sludge formation on the cathode, the melting or solidification of the freeze profile, will all break the material balance so that k_{ufeed} and k_{ofeed} cannot strictly satisfy (16). Therefore, the sets $\{f_{d1}\}$ and $\{f_{ifp}(S_{F_N})\}$ are distributed around the frequency f_{Thfeed}.

(2) In the 200-kA cells, $\{f_{d1}\}$, $\{f_{ifp}(S_{F_N})\}$ and f_{Thfeed} are all slightly larger than those in the 400-kA cells.

The sets $\{f_{d1}\}$ and $\{f_{ifp}(S_{F_N})\}$ of 400-kA cells are mainly distributed between 1.6×10^{-4} Hz and 6×10^{-4} Hz, while the corresponding range is between 3×10^{-4} Hz and 9×10^{-4} Hz for 200-kA cells. The frequency f_{Thfeed} for 400-kA cells is also less than that of 200-kA cells.

Equation (17) shows that the current intensity and the feed scheme jointly determine the theoretical-IFF f_{Thfeed}. The different values of f_{Thfeed} relate to the different distributive regions of the sets $\{f_{d1}\}$ and $\{f_{ifp}(S_{F_N})\}$.

Based on the above analysis, the alumina concentration sensitive frequency band of the NCV is defined as [0, f_{sens}] Hz, where

$$f_{sens} \equiv \sqrt{2} \cdot f_{Thfeed} \tag{18}$$

In Fig. 5, the frequencies f_{sens} of the 400-kA cell and the 200-kA cell are 7.0272×10^{-4} Hz and 9.3696×10^{-4} Hz, respectively. The sets $\{f_{d1}\}$ and $\{f_{ifp}(S_{F_N})\}$ are both almost in the range of the SFB, which means that the component associated with the alumina concentration in the NCV is in the range [0, f_{sens}]. Therefore, the upper limit, f_{sens} Hz, is the cutoff frequency for the low-pass filter in section IV.

Equations (17) and (18) show that the frequency band of the alumina concentration component in the NCV is related to I and $\tilde{s}_{feed}$, which means that the SFB depends on the current intensity and the feed scheme. Therefore, different low-pass filters for feed control should be designed for different SFBs to obtain the components related to the alumina concentration in the NCV. This conclusion is more general than the existing results in [7]; it represents a good foundation for the subsequent accurate acquisition of the alumina concentration component.

IV. PAC CALCULATION AND CONCENTRATION ESTIMATION BASED ON THE SFB

In this section, the general method based on translation-invariant filtering to acquire alumina concentration information in the NCV is given by using the alumina concentration sensitive frequency band. The optimal alumina concentration component obtained from the NCV is called the pseudo alumina concentration (PAC). Then, the estimated absolute concentration calculated from the PAC is verified by the measured alumina concentration in an industrial cell.

Since the time-frequency window of traditional filters (such as Kalman) is fixed, the limited ability of acquiring the ultralow-frequency signal component in the NCV is one obstacle. In recent years, multiresolution analysis (MRA) theory has also been used in the field of cell voltage (or resistance) analysis, such as the discrete wavelet transform (DWT) [21] and the wavelet-packet transform (WPT) [22], [23]. These methods are also not very suitable for analyzing alumina concentration information from the NCV. Because translation-invariant DWT (TIDWT) [24], [25] is insensitive to the starting point of the analyzed signal, it ensures the accuracy of the filtered signal. Its low-frequency and high-frequency components are both related to the zero-phase filter, and those components have the same length as the original signal, which can increase the low-frequency component information in its MRA and retain the corresponding relationship between time and the interesting low-frequency features in the original signal. Furthermore, TIDWT only performs the next decomposition with the low-frequency component. Fortunately, the information associated with the alumina concentration corresponds to the low-frequency components in the NCV (as shown in sections II and III), and the TIDWT, which requires $O(N \log_2 N)$ multiplications, has the same computational burden as the fast Fourier transform. Thus, TIDWT is more suitable for the acquisition of the alumina concentration component than DWT and WPT.

A. PAC CALCULATION ALGORITHM USING TIDWT

In this subsection, the SFB is used to determine the transform level J_0 of the partial TIDWT. To overcome the problem of subjectivity in filter selection, this study chooses the most suitable scaling filter by analyzing the properties of the wavelet basis, including vanishing moment, compact support, etc.

1) PASS-BAND DETERMINATION FOR THE TIDWT SCALING FILTER BASED ON THE SFB

The transform level J of the partial TIDWT is determined by the physical meaning of the original signal in the frequency domain. The nominal pass-band of the Jth-level scaling filter, which is an approximation of a low-pass filter, is given by [26]

$$0 \le |f| \le \frac{1}{4 \cdot \tau_J} \tag{19}$$

where $\tau_J = 2^{J-1}$.

Let $J_0 \in \mathrm{N}^+$ be the transform level of the partial TIDWT for the NCV. J_0 is then obtained by Equations (10), (17), (18) and (19),

$$\begin{cases} N_{Thbase} = \dfrac{s_{feed} \times 10^{-4}}{1.7617 \times I} \\ f_{Thfeed} = \dfrac{(1-\beta_u)(1+\beta_o)}{N_{Thbase} \cdot [k_{ufeed} \cdot (1+\beta_u) + k_{ofeed} \cdot (1-\beta_o)]} \\ f_{sens} = \sqrt{2} \cdot f_{Thfeed} \\ f_{filter} = \dfrac{f_s}{4 \cdot \tau_{J_0}} \\ J_0 = \arg\min(f_{sens} \le f_{filter}) \end{cases} \tag{20}$$

where $\tau_{J_0} = 2^{J_0-1}$.

The frequency range $[0, f_{filter}]$ is the pass-band of the scaling filter corresponding to the sampling frequency f_s.

TABLE 1. Wavelet comparison.

Filters	Haar	db2	la4
Vanishing moment	1	2	4
Support length	1	3	7
Number of boundary coefficients	64	190	442

The 5th formula in (20) denotes that the SFB determines the pass-band of the scaling filter, and then the level J_0 is obtained. Therefore, the levels of the 400-kA and 200-kA cells shown in Fig. 5 are $J_0 = 6$ and $J_0 = 5$, respectively.

2) SELECTION OF WAVELET FILTER FOR TIDWT

Vanishing moments and compact support are the important properties of a wavelet basis, and they have a close relationship when the wavelet bases are orthonormal. If an orthonormal wavelet has r vanishing moments, the support length is $L = 2r - 1$ [27]. The more vanishing moments there are, the better the transition approximates the original signal. However, an increased number of vanishing moments will inevitably lead to an increase in support length. TIDWT uses circular filtering, and the coefficients affected by the circularity are called boundary coefficients. The lengths of the jth-level TIDWT scaling and wavelet filters are both $L_j = (2^j - 1)(L - 1) + 1$; the number of boundary coefficients is $\min\{L_j - 1, N\}$, where N is the length of the filtered signal [24]. Consequently, when N is sufficiently large, the number of boundary coefficients increases with j and L. Therefore, when the transform level is fixed, the number of vanishing moments, support length and the number of boundary coefficients are the main properties that must be considered and weighed against each other when selecting the scaling and wavelet filters.

To make the extracted alumina concentration information in the NCV as accurate as possible, the influence of different filters on the calculated PAC accuracy is discussed from the perspective of the properties of the wavelet basis. Table 1 lists the vanishing moment, support length, and the number of boundary coefficients ($J_0 = 6$) of the commonly used scaling and wavelet filters such as Haar, db2, and la4. Fig. 6 compares the approximation performance and boundary coefficients of the level $J_0 = 6$ TIDWT for $U1$ using the filters in Table 1.

(1) Comparison of approximation performance

Fig. 6(b) expands these plots in the region $600 \le t \le 1000$. Table 1 and Fig. 6 show that la4 has the highest order vanishing moments, and the best approximation performance to $U1$. Especially when $U1$ is in the peaks and troughs (as in the vicinity of the abscissa values 750, 850 and 950 in Fig. 6(b)), la4 and db2 are significantly better than Haar.

(2) Comparison of boundary coefficients

Fig. 6(a) shows the beginning and end of the boundary coefficient regions of the filters in Table 1 using two vertical lines of the same color. For example, the boundary coefficient regions (yellow vertical lines) of the Haar filter are [0, 63] and [1377, 1440]. Fig. 6(a) shows that the number of boundary coefficients (green vertical lines) of la4 is the largest, and the number of boundary coefficients (blue vertical lines) of db2 is between that of the Haar and la4 filters.

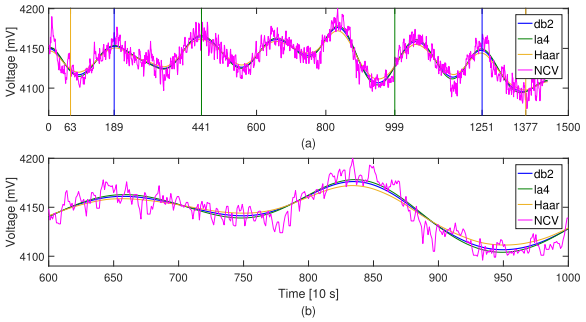

FIGURE 6. Performance comparison of the three filters in Table 1 (a) Comparison of the number of boundary coefficients; (b) expansion of $U1$ in the region $600 \le t \le 1000$.

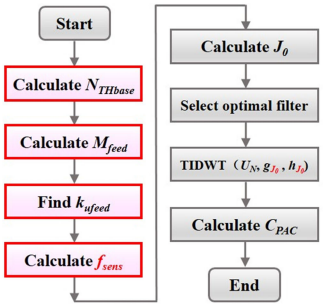

FIGURE 7. Flowchart of PAC calculation.

The transform of la4 is the closest to the original signal, but the boundary coefficient regions are larger. Although the boundary coefficient regions are the smallest when using Haar, they are accompanied by poor approximation performance, and serious energy leakage occurs because of the first-order vanishing moment [28]. Therefore, it is more suitable to use the db2 filter with two vanishing moments for the NCV.

3) ALGORITHM FOR PAC CALCULATION

Based on the above analysis, a general algorithm to obtain the alumina concentration information from the NCV for current intensity I, the feed scheme $\tilde{s}_{feed}$ and sampling frequency f_s is given. Fig. 7 shows the flowchart for calculating PAC. The steps in the red box constitute the work of the alumina SFB identification stage, and the steps in the gray box constitute the work of the PAC calculation stage using the TI method.

In the algorithm 1, the underfeed coefficient k_{ufeed} is obtained by the subfunction UFeedCoef; the filter coefficient of db2 is obtained by the subfunction WaveFilter; the subfunction TIFilter constructs the J_0 level TIDWT scaling and wavelet filters of db2; the subfunction ScaleCoef calculates the level J_0 db2 TIDWT-based scale coefficients; and the subfunction PAC calculates the PAC from the J_0th-level scale

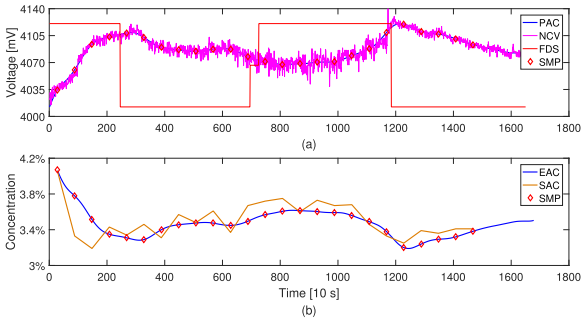

FIGURE 8. (a) NCV and feed state; (b) Estimation of the alumina concentration.

TABLE 2. Comparison of estimation errors.

Method	SFB-based TI Method	PSO LS-SVM [29]	Chaos-Opt NN [29]	ELM [30]	BP [30]	SVM [30]
RMSE (%)	0.13	0.07	0.09	13.58	16.91	13.76
ARE (%)	3.19	3.26	3.85	6.56	6.94	6.71

coefficients. The maximum number of multiplications in the algorithm PseudoAluCon is $O(N\log_2 N)$ when calculating the PAC corresponding to an NCV of length N.

Algorithm 1 PseudoAluCon Algorithm

procedure PseudoAluCon($U_N, F_N, I_b, f_s, \tilde{s}_{feed}, \beta_u, \beta_o$)
$N_{Thbase} \leftarrow \frac{\tilde{s}_{feed}\times 10^4}{1.7617\times I}$
$M_{feed} \leftarrow \text{IntegralFeedPeriod}(F_N, N_{Thbase}, k_1, k_2)$
$k_{ufeed} \leftarrow \text{UFeedCoef}(M_{feed}, N_{Thbase}, \beta_u)$
$f_{sens} \leftarrow \frac{\sqrt{2}\cdot(1-\beta_u^2)(1+\beta_o)}{N_{Thbase}\cdot k_{ufeed}\cdot(2-\beta_u^2-\beta_o^2)}$
$J_0 \leftarrow \arg\min(f_{sens} \le \frac{f_s}{2^{J_0+1}})$
$[g\ h] \leftarrow \text{WaveFilter}('db2')$
$[g_{J_0}\ h_{J_0}] \leftarrow \text{TIFilter}(g, h, J_0)$
$V_{J_0} \leftarrow \text{ScaleCoef}(U_N, g_{J_0}, h_{J_0})$
$C_{\text{PAC}} \leftarrow \text{PAC}(V_{J_0}, g_{J_0}, h_{J_0})$
return C_{PAC} ▷ The pseudo alumina concentration
end procedure

B. ESTIMATION OF THE ABSOLUTE CONCENTRATION

In this subsection, the absolute concentrations calculated from the PAC are validated using measured concentrations of electrolyte samples. The samples were obtained every 10 minutes for 4 hours, and there were a total of 25 samples. The sampling was performed in a cell for which the NCV and feed states had an approximate "under-rise and over-fall" relationship. The sampling process also avoided routine operation and special cell conditions.

Fig. 1 shows that in the low-concentration region, the theoretical cell voltage decreases with increasing alumina concentration. Therefore, after obtaining the PAC, invert the PAC and benchmark the results with the measured concentrations to obtain absolute concentration estimate values. Fig. 8(a) shows the NCV and feed state during sampling, where red diamonds denote the electrolyte sampling instant. In Fig. 8(b), the yellow curve is the measured absolute concentration, and the blue curve is the estimated absolute concentration calculated from the PAC. The proposed method can continuously track the alumina concentration without training, and the requirements on the number of data samples and the time complexity are lower than those of the methods in [29] and [30]. Table 2 compares the estimation errors of the methods of [29] and [30] with the proposed method. The maximum error is 0.46%, the root mean square error (RMSE) is 0.13%, and the average relative error (ARE) is 3.19%. In terms of error, the proposed method is better than that from [30], and the ARE is smaller than that in [29], but the RMSE is greater. The error of the proposed method is within acceptable limits.

According to the measured concentration verification, both in terms of time and accuracy, the PAC can well track the change in alumina concentration in the cell. Therefore, the relative concentration calculated from the PAC can better represent the real-time concentration change. The following section will illustrate that the relative concentration PAC-slope can improve the performance of feed control.

V. IMPROVEMENT OF THE FEED CONTROL PERFORMANCE

To compare the feed control performance using the PAC-slope with the slope, this section takes the routine feed control rules as an example for elaboration. The slope is collected from industrial cells and obtained by the multiple filter method.

Feed control is the most important component of a cell control system. Each major aluminum company has its own feed control strategy [3]–[6], [8]. Most of these feed control strategies have the routine feed control rules of underfeed and overfeed switching under normal alumina concentration conditions. Fig. 9 is a schematic diagram of routine feed control rules based on the filtered voltage U_{filter} and the slope G_{K0009}. The routine feed control rules can be briefly described as follows:

1) If $G^{(1)} > 0$ and $G = P_{uo}$, $B(k) = N_{ofeed}$, which means that the feed interval is switched from underfeed to overfeed;
2) If $G^{(2)} > 0$ and $G^{(1)} = 0$, $B(k) = N_{ufeed}$, which means that the feed interval is switched from overfeed to underfeed;
3) Otherwise, $B(k) = B(k-1)$, which means that the feed interval remains unchanged.

Fig. 10 shows the slope G_{K0009} and feed state F_{U1} corresponding to $U1$, which are collected from a 400-kA industrial cell. Fig. 10 depicts that, at the time of the rising slope, if $G_{K0009} = P_{uo}$, the feed interval is switched from underfeed to overfeed, as the sampling points $t = 169$ and $t = 636$ show. If the slope reaches a local minimum during the overfeed period, the feed interval is switched from overfeed to

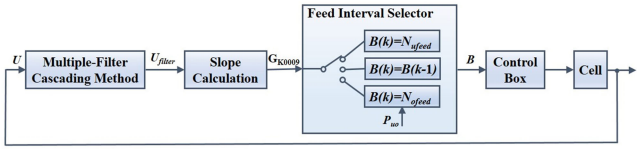

FIGURE 9. Schematic diagram of routine feed control rules based on the slope.

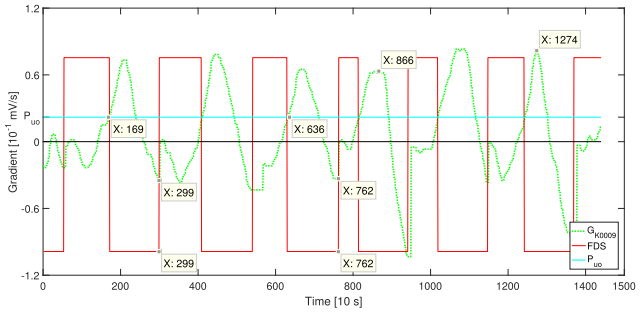

FIGURE 10. G_{K0009} and F_{U1}.

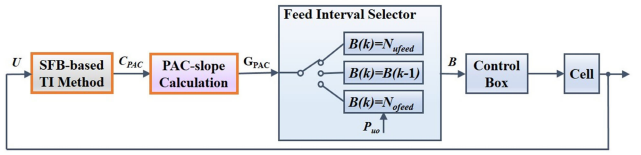

FIGURE 11. Schematic diagram of routine feed rules based on the PAC-slope.

underfeed, as the sampling points $t = 299$ and $t = 762$ show. It can be concluded that the number and appearance time of slopes that meet the switch conditions directly affect the accuracy and timeliness of feed control. To obtain the filtered voltage U_{filter}, the filter pass-band and filter coefficients are determined by experience or on-site experiments; the method of calculating the slope G_{K0009} from U_{filter} is relatively arbitrary. Thus, the filtered voltage and slope obtained in this way introduce certain hidden dangers to the timeliness and accuracy of feed control.

Fig. 11 shows a schematic diagram of routine feed rules based on the PAC-slope G_{PAC}. The orange boxes in Fig. 11 correspond to the orange dotted boxes in Fig. 4.

To elaborate the performance of feed control, the slopes of 400-kA and 200-kA cells collected on-site were compared with PAC-slopes. Moreover, the following provisions were made:

1) The PAC and its rate of change obtained from the NCV according to the SFB are represented by the PAC and PAC-slope G_{PAC}, respectively.
2) The NCV $U1$ of the 400-kA cell and the NCV $U4$ of the 200-kA cell using the frequency band $[0,\ 2 \times 10^{-3}]$ Hz obtained in [7] are subjected to translation-invariant filtering, and the filtered results and change rates are represented as T002 and G_{T002}, respectively. This frequency band is obtained by performing a Fourier transform on the cell voltage of a 160-kA cell.

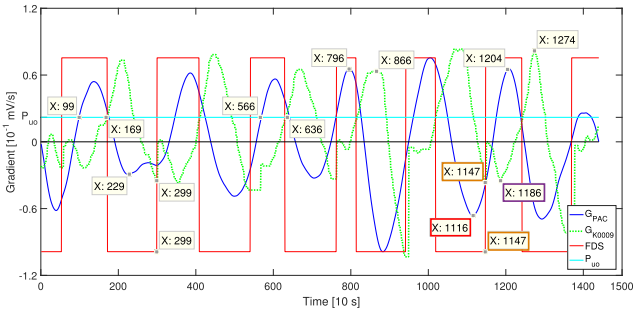

FIGURE 12. Timeliness improvement of feed control by using the PAC-slope.

3) Utilize SFB $[0,\ 9.3696 \times 10^{-4}]$ Hz of the 200-kA cell to perform translation-invariant filtering for $U1$ and $U4$. Here, the filtered results and change rates are represented as T0009 and G_{T0009}, respectively.
4) The slopes corresponding to $U1$ and $U4$ are recorded as G_{K0009}. To facilitate subsequent performance comparisons, G_{K0009} is shifted forward to obtain G'_{K0009}.
5) $G^{(1)}$ and $G^{(2)}$ are the first and second derivatives of G, respectively.
6) P_{uo} is the slope threshold for the switch of underfeed to overfeed.

In short, G_{PAC}, G_{T0009} and G_{T002} are obtained by translation-invariant filtering, and the slope G_{K0009} is obtained by the multiple filter method.

A. TIMELINESS IMPROVEMENT OF ROUTINE FEED CONTROL BY INTRODUCING TRANSLATION-INVARIANT FILTERING

The method of cascading multiple filters to obtain the filtered voltage U_{filter} has a delay and contains too much noise. Using such a filtered voltage to calculate the slope, the calculation method is relatively complicated, further exacerbating the delay. The green dashed line in Fig. 12 is the slope G_{K0009}, and the solid blue line is the PAC-slope G_{PAC}. Fig. 12 shows that, if the PAC-slope is used instead of the slope, at the sampling point $t = 99$ (corresponding to $t = 169$ in Fig. 10), the feed interval can switch from underfeed to overfeed; at the sampling point $t = 229$ (corresponding to Fig. 10 at $t = 299$), the feed interval can switch from overfeed to underfeed. Because translation-invariant filtering can reduce the delay in extracting ultralow-frequency information components from the original signal, the PAC can better track the alumina concentration information in the NCV, and the rate of change of the PAC (PAC-slope) G_{PAC} is simple to calculate and can also track the alumina concentration change in industrial cells in time. Therefore, with the PAC-slope used as the basis for feed control, the alumina concentration change can be tracked in time, and the 400-kA cell's feed control can be advanced by approximately 700 seconds. Similarly, it can advance the 200-kA cell's feed control by approximately 500 seconds (see Fig. 19 in the appendix).

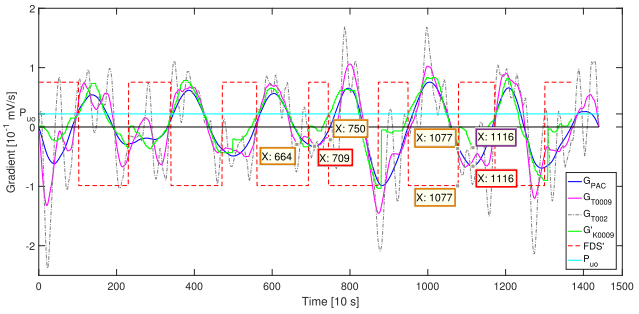

FIGURE 13. Accuracy improvement of feed control by using the PAC-slope.

Therefore, the introduction of translation-invariant filtering can alleviate the filtered signal lag caused by the multiple filter method, so that the PAC-slope can track the alumina concentration change in time, and thus the timeliness of the feed control can be improved. This makes feed control more sensitive, which in turn improves current efficiency and makes the alumina concentration fluctuate in a narrower range.

B. ACCURACY IMPROVEMENT OF ROUTINE FEED CONTROL BY INTRODUCING THE SFB

Fig. 12 shows that after the fifth slope peak, there are two local minimums $G_{K0009}(t = 1147)$ (yellow box label) and $G_{K0009}(t = 1186)$ (purple box label), which satisfy the switch condition of overfeed to underfeed. To ignore the effect of delay, G_{K0009} and FDS are moved forward by 70 sampling points to obtain G'_{K0009} and FDS' (square curve shown by the red dotted line), which is shown in Fig. 13. Fig. 13 shows that the local minimum value of $G_{PAC}(t = 1116)$ (red box label) on the PAC-slope corresponds to $G'_{K0009}(t = 1116)$ (Fig. 13) and $G_{K0009}(t = 1186)$ (Fig. 12) of the purple box label on the slope. From section IV's "B Estimation of the alumina absolute concentration," it can be known that the PAC can better track the change in alumina concentration, and the PAC-slope can represent the change in alumina concentration in the industrial cell. Therefore, the local minimum associated with the alumina concentration is $G_{K0009}(t = 1186)$ (purple box label) in Fig. 12, not $G_{K0009}(t = 1147)$ (yellow box label). Thus, it appears that when multiple points meet the underfeed/overfeed switch rule, the feed state switch is prone to being performed at the wrong time. Table 3 counts the number of sampling points that meet the underfeed/overfeed switch rule in the six IFPs in Fig. 13. From the above analysis, it can be inferred that the fewer the number of sampling points that meet the switch conditions, the more stable the feed control is. Fig. 13 and Table 3 show that

1) the change rate of G_{T002} is the most oscillating and cannot be directly used for feed control.
2) there are still significant oscillations in G_{T0009} and G'_{K0009}, resulting in multiple points of the change rates in Fig. 13 and Table 3 satisfying the switch condition. For example, only one point in the practical-IFP of $T_{ifp,U1}(1)$ and $T_{ifp,U1}(5)$ satisfies the switch condition. In the other four practical-IFPs, there are multiple points that satisfy the switch. In particular, $T_{ifp,U1}(3)$ and $T_{ifp,U1}(6)$ have 3 such points.
3) G_{PAC} has no significant oscillation, so only one point satisfies the switch condition in each of the practical-IFPs.

TABLE 3. Number of points that meet the underfeed/overfeed switch rule.

400-kA	$u \rightarrow o$: $G^{(1)} > 0$ and G=P_{uo}					
$T_{ifp,F1}(i)$	1	2	3	4	5	6
G_{PAC}	1	1	1	1	1	1
G_{T0009}	1	1	1	1	1	1
G_{T002}	2	2	2	1	2	1
G'_{K0009}	1	1	1	1	1	1
400-kA	$o \rightarrow u$: $G^{(1)} = 0$ and $G^{(2)} > 0$					
$T_{ifp,F1}(i)$	1	2	3	4	5	6
G_{PAC}	1	1	1	1	1	1
G_{T0009}	1	2	3	2	1	3
G_{T002}	3	2	3	2	4	3
G'_{K0009}	2	2	2	2	2	2

The reason that multiple points meet the switch condition is that the filter has a wider pass-band, which causes the filtered result and its change rate to still contain excessive noise. Because the proposed SFB can yield a narrower pass-band of the filter, the use of SFB can filter out the components that are not related to the alumina concentration in the NCV as much as possible. Thus, the PAC and PAC-slope can reduce the complexity of the feed control algorithm and can better track the changes in the alumina concentration in an industrial cell, making feed control more accurate.

C. UNIVERSALITY IMPROVEMENT OF THE RELATIVE CONCENTRATION ESTIMATION BY INTRODUCING THE SFB

This subsection takes the NCV $U4$ of a 200-kA cell as an example (see Fig. 18 in the appendix) and then compares it with the result of the NCV $U1$ of the 400-kA cell to analyze the influence of the SFB on industrial cells of different current intensities and feed schemes.

By using the same method as above with a 200-kA cell, the slope G_{K0009} collected from an industrial cell is lagging the PAC-slope G_{PAC} (G_{T0009}) by approximately 50 sampling points (see Fig. 19 in the appendix). Therefore, the FDS and slope G_{K0009} corresponding to the NCV $U4$ of the 200-kA cell are shifted forward by 50 sampling points to obtain the FDS' (square curve shown by the red dashed line) and G'_{K0009} in Fig. 14. Table 7 counts the number of sampling points that meet the underfeed/overfeed switch rule. The magenta curves in Fig. 13 and Fig. 14 are obtained by translation-invariant filtering with $[0, 9.3696 \times 10^{-4}]$ Hz as the pass-band. The difference is that $[0, 9.3696 \times 10^{-4}]$ Hz is only the SFB of the 200-kA cell, not the SFB of the 400-kA cell. In Fig. 14,

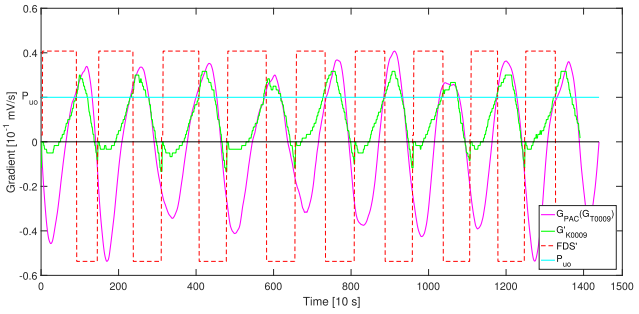

FIGURE 14. G_{PAC} of 200-kA.

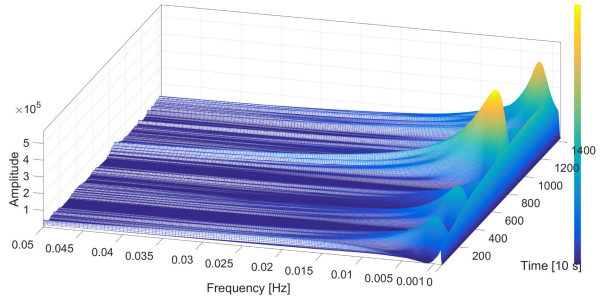

FIGURE 15. Energy distribution of $U1$ in [0, 0.05] Hz.

G_{PAC} (G_{T0009}) of the 200-kA cell has only one point that satisfies the switch condition in each IFP, while G_{T0009} of the 400-kA cell shown in Fig. 13 has multiple points in each IFP that satisfy the switch condition. For example, after the third peak in Fig. 13, G_{T0009} has three local minimums, $G_{T0009}(t = 664)$, $G_{T0009}(t = 709)$ and $G_{T0009}(t = 750)$, among which only $G_{T0009}(t = 709)$ is related to the alumina concentration that coincides with the PAC-slope local minimum $G_{T0009}(t = 709)$. Therefore, the other two local minimums significantly interfere with the judgment of the feed state switch point. Obviously, G_{PAC} obtained from the 400-kA cell with an SFB of $[0, 7.0272 \times 10^{-4}]$ Hz has only one point in each IFP that satisfies the switch rule.

The SFB is more universal than the pass-band obtained from experience, which can significantly reduce the incorrect decision of the feed control system of different current intensity cells without changing the control rules. The introduction of translation-invariant filtering can significantly decrease the delay caused by the multiple filter method. Therefore, compared with the filtered voltage U_{filter} and slope G_{K0009}, the PAC and PAC-slope can control the feed operation with more accuracy and timeliness, which can stabilize the cell condition and improve the current efficiency at the lowest cost.

VI. CONCLUSION

This study proposes an alumina concentration estimation method based on sensitive frequency band identification using marginal kurtosis, which adapts to the frequent cell condition changes in an industrial cell. As verified by the measured concentration, the average relative error of the estimated absolute concentration is 3.19%. Compared with the slope obtained by the previous method, the PAC-slope can advance the feed control operation by 500 to 700 seconds and significantly reduces the number of points that satisfy the underfeed/overfeed switch rules. The main contributions, all of which have improved the feed control performance, are as follows.

1) Marginal kurtosis and the marginal kurtosis dominant frequency are proposed and used to accurately capture the frequency band in which the normalized cell voltage energy accumulates. Comparative experiments show that marginal kurtosis is more suitable than the power spectrum density and spectral kurtosis to analyze complex signals with energy concentrated in nonsingular signal components, which is a useful supplement to the last two methods.
2) The practical integrated feed frequency and its formal expression are proposed, providing the tools for automatic analysis of a large number of feed states.
3) The theoretical integrated feed frequency is proposed, and its calculation formula is derived. Equation (17) shows that the theoretical integrated feed frequency under ideal conditions is directly proportional to the current intensity I and inversely proportional to the feed scheme $\tilde{s}_{feed}$.
4) Using marginal kurtosis and integrated feed frequency to identify the sensitive frequency band of the alumina concentration, a general conclusion related to feed control of industrial cells can be made: the sensitive frequency bands of the alumina concentration vary with the current intensity and the feed scheme, which means that different filter pass-bands should be used to filter the NCV to obtain the critical parameters for feed control.
5) Based on the SFB of the alumina concentration, the calculation formula of the filter pass-band used to filter the NCV is obtained, the application of which can change the current situation of obtaining the filter pass-band through experience or on-site experiments.
6) Based on the alumina concentration SFB, vanishing moments, compact support and boundary coefficients, etc., the most suitable translation-invariant filter is determined, and a general algorithm for acquiring the PAC is designed. Using the PAC, the absolute and relative concentrations of alumina can be estimated.
7) The relative concentration PAC-slope for feed control has been obtained by using the PAC, which greatly decreases the serious delay of the filtered voltage and slope caused by the multiple filter method, so that the feed control can closely keep up with the changes in the alumina concentration.

APPENDIX

A. THE ENERGY DISTRIBUTION OF NCV U1 WITHIN THE EFFECTIVE BAND [0, 0.05] HZ IN A 400-kA CELL

Fig. 15 corresponds to subsection "1) Definition of MK" in the text. Fig. 15 shows the integral wavelet transform ampli-

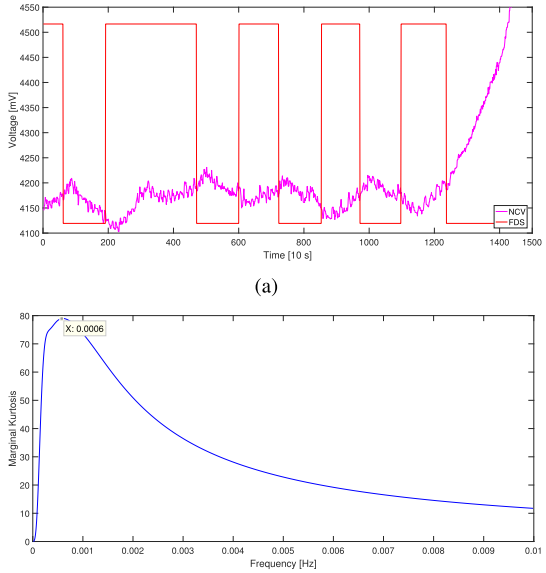

FIGURE 16. Analysis of $U2$ (a) $U2$; (b) Marginal kurtosis.

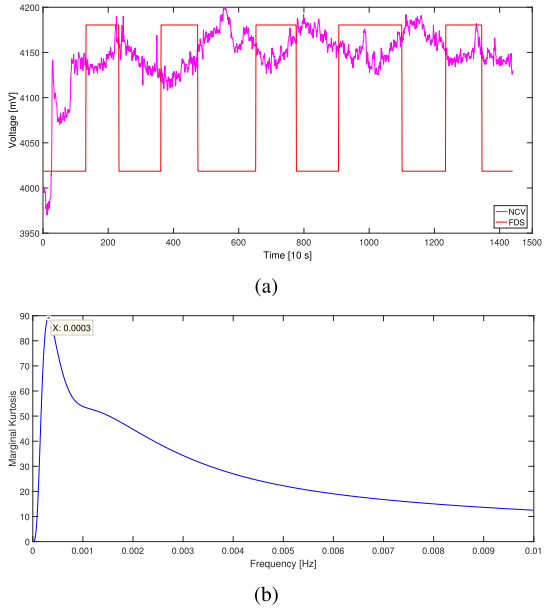

FIGURE 17. Analysis of $U3$ (a) $U3$; (b) Marginal kurtosis.

tude of $U1$ in the effective band [0, 0.05] Hz. The amplitude is small in [0, 0.05] Hz, while high in the low-frequency band [0, 0.01] Hz. Fig. 2(b) in the text is a partial view of $U1$ in [0, 0.01] Hz. Fig. 15 and Fig. 2(b) show that $U1$ has distinct time-frequency properties in the high- and low-frequency bands. The energy is concentrated in the low-frequency region, and the amplitude has no obvious singular value.

B. ANALYSIS OF U2 PRIOR TO THE ANODE EFFECT IN A 400-kA CELL

Fig. 16 corresponds to subsection "3) MK-DF of the NCV with various cell conditions", in the text. Fig. 16 is an analysis of the NCV $U2$ and feed state before the anode effect, which satisfies the "under-rise and over-fall" relationship. In Fig. 16(b), there is only one maximum at $f_{d1} = 0.0006$ Hz.

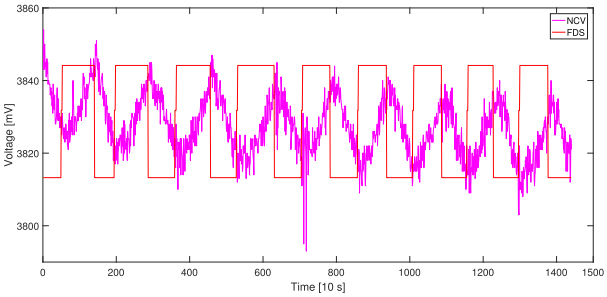

FIGURE 18. $U4$.

TABLE 4. MK-DFs of the NCVs under normal cell conditions.

NCV No.	$U1\_1$	$U1\_2$	$U1\_3$	$U1\_4$	$U1\_5$
MK-DF1	3.536e-4	3.664e-4	3.141e-4	3.333e-4	3.934e-4
MK-DF2	1.947e-3	1.611e-3	2.115e-3	/	/
NCV No.	$U1\_6$	$U1\_7$	$U1\_8$	$U1\_9$	$U1\_10$
MK-DF1	4.125e-4	4.535e-4	3.255e-4	4.429e-4	5.272e-4
MK-DF2	/	/	2.192e-3	/	2.140e-3
NCV No.	$U1\_11$	$U1\_12$	$U1\_13$	$U1\_14$	$U1\_15$
MK-DF1	3.373e-4	5.166e-4	3.981e-4	3.372e-4	4.028e-4
MK-DF2	/	2.312e-3	/	2.090e-3	2.090e-3

TABLE 5. MK-DFs of the NCVs prior to the anode effects.

NCV No.	$U2\_1$	$U2\_2$	$U2\_3$	$U2\_4$	$U2\_5$
MK-DF1	3.294e-4	4.986e-4	3.179e-4	5.956e-4	4.14e-4
MK-DF2	/	/	/	/	1.432e-3
NCV No.	$U2\_6$	$U2\_7$	$U2\_8$	$U2\_9$	$U2\_10$
MK-DF1	3.578e-4	2.703e-4	3.536e-4	3.179e-4	2.861e-4
MK-DF2	/	2.072e-3	/	2.527e-3	2.687e-3
NCV No.	$U2\_11$	$U2\_12$	$U2\_13$	$U2\_14$	$U2\_15$
MK-DF1	3.086e-4	2.300e-4	3.146e-4	3.536e-4	4.869e-4
MK-DF2	1.867e-3	1.683e-3	1.699e-3	/	/

C. ANALYSIS OF U3 AFTER THE METAL TAPPING OPERATION IN A 400-kA CELL

Fig. 17 corresponds to subsection "3) MK-DF of the NCV with various cell conditions", in the text. Fig. 17 is an analysis of the NCV $U3$ and feed state after the metal tapping operation, which satisfies the "under-rise and over-fall" relationship. In Fig. 17(b), there is only one maximum at $f_{d1} = 0.0003$.

D. MK-DFs OF THE NCVs PRIOR TO THE ANODE EFFECT AND AFTER THE METAL TAPPING OPERATION IN 400-kA CELLS

These tables correspond to subsection "3) MK-DF of the NCV with various cell conditions", in the text. Tables 4, 5, and 6 show that almost all NCVs analyzed have an MK-DF

TABLE 6. MK-DFs of the NCVs after the metal tapping operation.

NCV No.	$U3\_1$	$U3\_2$	$U3\_3$	$U3\_4$	$U3\_5$
MK-DF1	2.823e-4	3.578e-4	2.725e-4	4.174e-4	2.996e-4
MK-DF2	2.017e-3	/	1.592e-3	1.555e-3	/
NCV No.	$U3\_6$	$U3\_7$	$U3\_8$	$U3\_9$	$U3\_10$
MK-DF1	4.812e-4	3.453e-4	3.708-4	4.535e-4	3.621e-4
MK-DF2	2.066e-3	2.017e-3	/	/	1.611e-3
NCV No.	$U3\_11$	$U3\_12$	$U3\_13$	$U3\_14$	$U3\_15$
MK-DF1	3.752 e-4	4.755e-4	4.481e-4	4.174e-4	4.377e-4
MK-DF2	1.709e-3	1.994e-3	/	/	/

TABLE 7. Number of points that meet the underfeed/overfeed switch conditions.

200-kA	$u \rightarrow o$: $G^{(1)} > 0$ and G=P_{uo}							
$T_{ifp,U4}(i)$	1	2	3	4	5	6	7	8
$G_{PAC}(G_{T0009})$	1	1	1	1	1	1	1	1
G_{T002}	3	1	2	3	1	2	2	1
G'_{K0009}	1	1	1	1	1	1	2	1
200-kA	$o \rightarrow u$: $G^{(1)} = 0$ and $G^{(2)} > 0$							
$T_{ifp,U4}(i)$	1	2	3	4	5	6	7	8
$G_{PAC}(G_{T0009})$	1	1	1	1	1	1	1	1
G_{T002}	1	2	2	3	2	2	2	2
G'_{K0009}	3	2	2	2	2	2	2	2

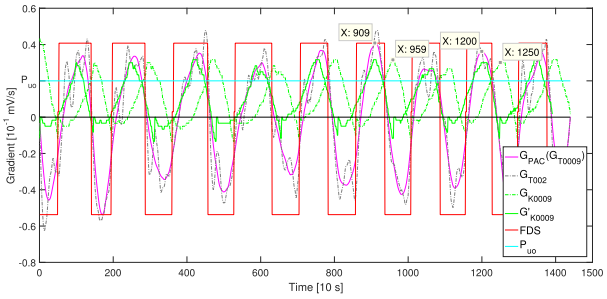

FIGURE 19. Change rates of the components of $U4$ obtained by various filter bands.

below 0.001 Hz, and some NCVs have a second MK-DF above 0.001 Hz.

E. NCV OF THE 200-kA CELL

This is related to subsection "C. Universality improvement of the relative concentration estimation by introducing the SFB" in the text. Fig. 18 shows the NCV $U4$ and FDS of a 200-kA cell where the sampling frequency is 0.1 Hz and $N = 1440$, which have the "under-rise and over-fall" relationship. Fig. 18 shows there are eight complete practical-IFPs.

In Fig. 19, G_{PAC} is the change in PAC with time. The other notations in Fig. 19 and Table 7 have the same meaning as in Fig. 13 and Table 3, except they are associated with $U4$. A separate analysis of Fig. 19 and Table 7 reveals a similar conclusion regarding the 400-kA cell, especially in $T_{ifp,U4}(7)$, where there are two points that satisfy the switch rule of underfeed to overfeed for G'_{K0009}, but only one point for G_{PAC}.

REFERENCES

[1] P. Lavoie, M. P. Taylor, and J. B. Metson, "A review of alumina feeding and dissolution factors in aluminum reduction cells," *Metall. Mater. Trans. B*, vol. 47, no. 4, pp. 2690–2696, May 2016.
[2] H. Vogt, "On the various types of uncontrolled potential increase in electrochemical reactors—The anode effect," *Electrochimica Acta*, vol. 87, pp. 611–618, Jan. 2013.
[3] P. by Bonny, J. L. Gerphagnon, and G. Laboure, "Process and apparatus for accurately controlling the rate of introduction and the content of alumina in an igneous electrolysis tank in the production of aluminium," U.S. Patent 4 431 491, Feb. 14, 1984.
[4] D. A. Simakov, A. O. Gusev, and K. B. Bakin, "Method for controlling an alumina feed to electrolytic cells for producing aluminum," U.S. Patent 2017 145 574 A1, May 25, 2017.
[5] S. Fardeau and B. Sulmont, "Method of producing aluminium in an electrolysis cell," U.S. Patent 8 961 773, Feb. 24, 2015.
[6] W. D. McGraw, K. G. Christian, and W. M. Hall, "Estimation and control of alumina concentration in hall cells," U.S. Patent 4 814 050, Mar. 21, 1989.
[7] J. Li, Y. X. Liu, and Y. Z. Huang, "Studies on the modelling of control signal filtering and noise analysis for the aluminium electrolytic process," *J. Central South Inst. Mining Metall.*, vol. 24, no. 3, pp. 318–325, Jun. 1993.
[8] G. I. Blatch, M. P. Taylor, and M. F. Slengarry, "Process for controlling aluminum smelting cells," U.S. Patent 5 089 09, Feb. 18, 1992.
[9] J. Antoni, "Fast computation of the kurtogram for the detection of transient faults," *Mech. Syst. Signal Process.*, vol. 21, no. 1, pp. 108–124, Jan. 2007.
[10] T. Barszcz and A. Jabáski, "A novel method for the optimal band selection for vibration signal demodulation and comparison with the kurtogram," *Mech. Syst. Signal Process.*, vol. 25, no. 1, pp. 431–451, Jan. 2011.
[11] J.-H. Lee, D.-H. Kim, and Y.-H. Shin, "Hyperbolic localization of incipient tip vortex cavitation in marine propeller using spectral kurtosis," *Mech. Syst. Signal Process.*, vol. 110, pp. 442–457, Sep. 2018.
[12] B. J. Welch, "Technology of electrolytic reduction of alumina by the Hall-Heroult process. PT. 1. A voltage analysie under conditions of varying alumina concentration," *Australas. Inst. Mining Metles*, vol. 214, pp. 1–19, Dec. 1965.
[13] M. C. Schneller, "*in situ* alumina feed control," *JOM*, vol. 61, no. 11, pp. 26–29, Nov. 2009.
[14] M. Schneller, "Aluminum production process control," U.S. Patent 8 052 859, Nov. 8, 2011.
[15] K. Zhou, Z. Lin, D. Yu, B. Cao, Z. Wang, and S. Guo, "Cell resistance slope combined with LVQ neural network for prediction of anode effect," in *Proc. 6th Int. Conf. Intell. Control Inf. Process. (ICICIP)*, Wuhan, China, Nov. 2015, pp. 47–51.
[16] W. E. Haurpin, "Polarization in an aluminum reduction cell," *J. The Electrochem. Soc.*, vol. 103, no. 3, pp. 174–178, Mar. 1956.
[17] H. Kvande and W. Haupin, "Cell voltage in aluminum electrolysis: A practical approach," *JOM*, vol. 52, no. 2, pp. 31–37, Feb. 2000.
[18] L. Banta, C. Dai, and P. Biedler, "Noise classification in the aluminum reduction process," in *Proc. Essential Readings Light Met.*, 2016, pp. 812–816.
[19] Y.-L. Wang, J. Tie, G.-F. Tu, S.-C. Sun, R.-T. Zhao, and Z.-F. Zhang, "Effect of gas bubble on cell voltage oscillations based on equivalent circuit simulation in aluminum electrolysis cell," *Trans. Nonferrous Met. Soc. China*, vol. 25, no. 1, pp. 335–344, Jan. 2015.
[20] Z. Shuiping and D. Lei, "Frequency characteristic and its application of the cell resistance in aluminum electrolysis," in *Proc. 7th Int. Conf. Comput. Sci. Edu. (ICCSE)*, Melbourne, VIC, Australia, Jul. 2012, pp. 165–168.
[21] B. C. Li, J. S. Chen, and X. J. Zhai, "Cell voltage noise reduction based on wavelet in aluminum reduction cell," in *Light Metals*. Cham, Switzerland: Springer, 2011, pp. 599–601.
[22] A. Verdenik, "Analysis and visualization of aluminum reduction cell noise based on wavelet transform," in *Light Metals*. Hoboken, NJ, USA: Wiley, 2016, pp. 403–408.
[23] D. K. Alves, F. B. Costa, R. Lucio de Araujo Ribeiro, C. Martins de Sousa Neto, and T. de Oliveira Alves Rocha, "Real-time power measurement using the maximal overlap discrete wavelet-packet transform," *IEEE Trans. Ind. Electron.*, vol. 64, no. 4, pp. 3177–3187, Apr. 2017.

[24] J. Liang and T. W. Parks, "A translation-invariant wavelet representation algorithm with applications," *IEEE Trans. Signal Process.*, vol. 44, no. 2, pp. 225–232, Feb. 1996.
[25] T. J. Rato, J. Blue, J. Pinaton, and M. S. Reis, "Translation-invariant multi-scale energy-based PCA for monitoring batch processes in semiconductor manufacturing," *IEEE Trans. Autom. Sci. Eng.*, vol. 14, no. 2, pp. 894–904, Apr. 2017.
[26] S. G. Mallat, "Multiresolution approximations and wavelet orthonormal bases of $L^2(R)$," *Trans. Amer. Math. Soc.*, vol. 315, no. 1, pp. 69–87, Sep. 1989.
[27] I. Daubechies, "Orthonormal bases of compactly supported wavelets," *Commun. Pure Appl. Math.*, vol. 41, no. 7, pp. 909–996, Oct. 1988.
[28] I. Daubechies, "Regularity or vanishing moments," in *Ten Lectures on Wavelets*. Philadelphia, PA, USA: Society for Industrial and Applied Mathematics, 1992, pp. 242–249.
[29] G. Yan and X. Liang, "Predictive models of aluminum reduction cell based on LS-SVM," in *Proc. Int. Conf. Digit. Manuf. Autom.*, Dec. 2010, pp. 99–102.
[30] S. Zhang, Q. Yang, Y. Yin, and B. Cao, "A novel on-line alumina concentration measurement system," in *Proc. IEEE Int. Conf. Mechatronics Autom. (ICMA)*, Aug. 2015, pp. 362–368.

ZHAOHUI ZENG received the M.S. degree in computer software and theory from Xiangtan University, Xiangtan, China, in 2007. She is currently pursuing the Ph.D. degree in computer science and technology with Central South University, Changsha, China.

Her current research interests include knowledge automation, industrial big data analysis, fault diagnoses, and wavelet analysis theory and application.

WEIHUA GUI received the B.S. degree in electrical engineering and the M.S. degree in control engineering from Central South University, Changsha, China, in 1976 and 1981, respectively.

He was a Visiting Scholar with the Universität GH Duisburg, Duisburg, Germany, from 1986 to 1988. Since 1991, he has been a Full Professor with Central South University. Since 2013, he has been an Academician of the Chinese Academy of Engineering, Beijing, China. His current research interests include modeling and optimal control of complex industrial processes, fault diagnoses, and knowledge automation.

LIHUI CEN received the B.S. and M.S. degrees in control science and engineering from Central South University, Changsha, China, in 2000 and 2003, respectively, and the Ph.D. degree from the Department of Automation, Shanghai Jiao Tong University.

She is currently an Associate Professor with the School of Automation, Central South University. Her research interests include model predictive control, machine learning, and their applications in industrial processes.

XIAOFANG CHEN received the M.S. and Ph.D. degrees in control science and engineering from Central South University, Changsha, China, in 2000 and 2004, respectively.

He is currently a Full Professor with the School of Automation, Central South University. His current research interests include intelligent modeling and optimal control of complex industrial processes and knowledge driven manufacturing.

YONGFANG XIE received the B.S., M.S., and Ph.D. degrees in control science and engineering from Central South University, Changsha, China, in 1993, 1996, and 1999, respectively.

From 1999 to 2003, he was with the Tokyo International Information Science Research Institute, Tokyo, Japan, and was also a Visiting Scholar with the PToPA Research Institute, Tokyo. He is currently a Full Professor with the School of Automation, Central South University. His current research interests include modeling and optimal control of complex industrial processes, distributed robust control, and knowledge automation. He was a recipient of the China National Funds for Distinguished Young Scientists.